


SCIENTIFIC REPORTS



OPEN

First-principles investigation of the micromechanical properties of fcc-hcp polymorphic high-entropy alloys

Xiaoqing Li^{1,2,3}, Douglas L. Irving² & Levente Vitos^{1,3,4} 

High-entropy alloys offer a promising alternative in several high-technology applications concerning functional, safety and health aspects. Many of these new alloys compete with traditional structural materials in terms of mechanical characteristics. Understanding and controlling their properties are of the utmost importance in order to find the best single- or multiphase solutions for specific uses. Here, we employ first-principles alloy theory to address the micro-mechanical properties of five polymorphic high-entropy alloys in their face-centered cubic (fcc) and hexagonal close-packed (hcp) phases. Using the calculated elastic parameters, we analyze the mechanical stability, elastic anisotropy, and reveal a strong correlation between the polycrystalline moduli and the average valence electron concentration. We investigate the ideal shear strength of two selected alloys under shear loading and show that the hcp phase possesses more than two times larger intrinsic strength than that of the fcc phase. The derived half-width of the dislocation core predicts a smaller Peierls barrier in the fcc phase confirming its increased ductility compared to the hcp one. The present theoretical findings explain a series of important observations made on dual-phase alloys and provide an atomic-level knowledge for an intelligent design of further high-entropy materials.

There has been a notable increase of interest in the high-entropy alloys (HEAs) in the last years due to their outstanding properties^{1–12}, e.g., excellent strength and fracture toughness, high hardness, good wear and corrosion resistance, and good thermal conductivity. The HEAs contain several elements in equimolar or near equimolar ratios that often possess different ground state crystal structures. However, the majority of these reported alloys exhibit two simple structures, i.e., face-centered cubic (fcc) or body-centered cubic (bcc), whereas only few single-phase HEAs with hexagonal close-packed (hcp) structure have been produced^{13–16}. Among those, the hcp HEAs containing rare earth elements did not show compositional segregation, e.g., DyGdHoTbY, but they typically lacked pronounced solid-solution hardening due to the similar size and electronic structure of the constituents. Attempts to synthesize single-phase hcp HEAs without rare earth elements have been rare until now¹⁶ owing to compositional segregation¹⁷.

Recently, Li *et al.*^{6,12} developed a new class of HEAs, which exhibits an fcc and hcp phase mixture, such as Cr₁₀Mn₃₀Fe₅₀Co₁₀. These so-called dual phase HEAs display a combination of high strength and good ductility opposite to the single-phase fcc HEAs with similar components. Lately, an fcc to hcp phase transformation of Cr₂₀Mn₂₀Fe₂₀Co₂₀Ni₂₀ and Cr₂₅Fe₂₅Co₂₅Ni₂₅ under pressure was reported^{18–20}. Remarkably, the hcp phase was retained following decompression to ambient pressure, possibly opening a new, fruitful route for producing HEAs in the hcp structure. Furthermore, finite temperature *ab initio* calculations suggested that the free energy of hcp Cr₂₅Fe₂₅Co₂₅Ni₂₅ and Cr₂₀Mn₂₀Fe₂₀Co₂₀Ni₂₀ is lower than that of fcc at room temperature and below^{21,22}.

Mechanical properties of engineering materials are of primary interest because they determine the ability to withstand loads without failure. To further develop high-performance HEAs, it is fundamentally interesting to

¹Department of Materials Science and Engineering, KTH-Royal Institute of Technology, 10044, Stockholm, Sweden.

²Department of Materials Science and Engineering, North Carolina State University, Raleigh, North Carolina, 27695, USA. ³Research Institute for Solid State Physics and Optics, Wigner Research Center for Physics, P.O. Box 49, Budapest, H-1525, Hungary. ⁴Department of Physics and Astronomy, Division of Materials Theory, Uppsala University, Box 516, SE-75120, Uppsala, Sweden. Correspondence and requests for materials should be addressed to X.L. (email: xiaoqli@kth.se)

HEA	fcc			hcp			
	a_{EMTO}	a_{VASP}	$a_{\text{Expt.}}$	a_{EMTO}	$a_{\text{Expt.}}$	c_{EMTO}	$c_{\text{Expt.}}$
Cr ₁₀ Mn ₃₀ Fe ₅₀ Co ₁₀	3.503	2.478	...	3.948	...
Cr ₂₀ Mn ₂₀ Fe ₃₄ Co ₂₀ Ni ₆	3.517	2.487	...	3.979	...
Cr ₂₀ Mn ₂₀ Fe ₃₀ Co ₂₀ Ni ₁₀	3.519	2.488	...	3.985	...
Cr ₂₀ Mn ₂₀ Fe ₂₀ Co ₂₀ Ni ₂₀	3.529	3.540 ²⁵	3.597 ²⁵	2.493	2.544(1) ¹⁸	4.005	4.142(3) ¹⁸
			3.597 ¹⁸		2.535(2) ¹⁹		4.138(1) ¹⁹
Cr ₂₅ Fe ₂₅ Co ₂₅ Ni ₂₅	3.529	3.540 ²⁵	3.575 ²⁵	2.497	2.522 ²⁰	4.025	4.118 ²⁰
			3.574 ²⁰				

Table 1. Computed lattice parameters (in Å) as well as available theoretical and experimental data^{18–20,25} of HEAs in the hcp and fcc phases.

HEA	fcc			hcp				
	C_{11}	C_{12}	C_{44}	C_{11}	C_{12}	C_{13}	C_{33}	C_{44}
Cr ₁₀ Mn ₃₀ Fe ₅₀ Co ₁₀	258.4	137.6	205.0	484.5	215.0	132.2	573.8	142.3
Cr ₂₀ Mn ₂₀ Fe ₃₄ Co ₂₀ Ni ₆	255.3	152.5	190.6	429.9	197.5	110.9	498.1	117.5
Cr ₂₀ Mn ₂₀ Fe ₃₀ Co ₂₀ Ni ₁₀	250.0	150.5	186.6	415.9	190.3	104.6	478.7	111.6
Cr ₂₀ Mn ₂₀ Fe ₂₀ Co ₂₀ Ni ₂₀	240.0	146.9	179.3	375.6	179.1	90.1	433.8	96.8
Cr ₂₅ Fe ₂₅ Co ₂₅ Ni ₂₅	268.2	175.9	175.7	348.6	182.1	93.1	412.5	81.9

Table 2. Single-crystal elastic constants (in GPa) of HEAs in the hcp and fcc phases.

explore the mechanical properties of these polymorphic HEAs in both the fcc and hcp phases. However, difficulties in preparing pure phase samples have largely prevented the experimental characterization of the individual phases in dual phase HEAs hitherto, and a comparison of the mechanical properties of the two phases is still lacking. Here, using first-principles simulations, we compare for the first time the elastic properties and intrinsic shear strength of five polymorphic HEAs, namely, Cr₂₅Fe₂₅Co₂₅Ni₂₅, Cr₂₀Mn₂₀Fe₂₀Co₂₀Ni₂₀, Cr₂₀Mn₂₀Fe₃₀Co₂₀Ni₁₀, Cr₂₀Mn₂₀Fe₃₄Co₂₀Ni₆, and Cr₁₀Mn₃₀Fe₅₀Co₁₀, in their fcc and hcp phases. These five 3d transition metal HEAs were successfully synthesized, and their magnetic properties were characterized^{16,12,23,24}. Using the obtained shear strength, we lend fundamental insight into the half-width of the dislocation core that is involved in studying the plastic deformation behavior of these materials.

Results and Discussion

Lattice parameters. Table 1 lists the calculated equilibrium lattice parameters as well as available theoretical and experimental data^{18–20,25}. For the fcc phase, we can see that our values are very similar to the presented theoretical data calculated by the Vienna ab initio simulation package (VASP) using special quasi-random structures²⁵. Both theoretical results are in good agreement with the experimental values^{20,25}. For the hcp phase, our data agree well with the available experimental data^{18–20}.

Elastic properties. For a cubic crystal, there are three independent single-crystal elastic constants, i.e., C_{11} , C_{12} , and C_{44} . However, for a hexagonal solid, this number increases to five, namely C_{11} , C_{12} , C_{13} , C_{33} , and C_{44} . In addition, $C_{66} = (C_{11} - C_{12})/2$ holds. The obtained elastic constants for the five considered HEAs in their fcc and hcp phases are presented in Table 2. We find that both the fcc and hcp phases of all considered HEAs are elastically stable at zero temperature and pressure judged from the Born criteria^{26,27}. The elastic stability is consistent with their experimental observations at zero pressure and room temperature^{6,12,18,19}. Moreover, it was found that our obtained elastic constants for Cr₂₅Fe₂₅Co₂₅Ni₂₅ and Cr₂₀Mn₂₀Fe₂₀Co₂₀Ni₂₀ in their fcc phase agree well with recently reported theoretical data²⁸.

Using the obtained elastic constants, we calculated the single-crystal Young's modulus E in several high-symmetry directions and determined its anisotropy characterized by the anisotropy factor f_E defined in refs^{29,30}. f_E can be obtained from the following equations,

$$f_E^{\text{hcp}} = \frac{C_{33}C_{11} - C_{13}^2}{C_{11}^2 - C_{12}^2}, \quad (1)$$

$$f_E^{\text{fcc}} = \frac{2C_{44}(C_{11} + 2C_{12})}{C_{11}(C_{11} + C_{12}) - 2C_{12}^2}. \quad (2)$$

A larger deviation of f_E from 1 indicates a larger dependence of E on the loading direction.

For the fcc phase, we can see from Table 3 that the [111] and [001] directions possess the largest and smallest E , respectively. From the listed f_E^{fcc} , it is evident that E of Cr₂₀Mn₂₀Fe₂₀Co₂₀Ni₂₀ is the most anisotropic, whereas Cr₁₀Mn₃₀Fe₅₀Co₁₀ is the most isotropic alloy. For the hcp phase, E along the [0001] direction is larger than that along the $[2\bar{1}\bar{1}0]$ direction, and the largest f_E^{hcp} is found in Cr₂₅Fe₂₅Co₂₅Ni₂₅. The full directional dependence of

HEA	fcc					hcp			
	$E_{[001]}$	$E_{[110]}$	$E_{[111]}$	f_E^{fcc}	A_u	$E_{[2\bar{1}10]}$	$E_{[0001]}$	f_E^{hcp}	A_u
Cr ₁₀ Mn ₃₀ Fe ₅₀ Co ₁₀	162.7	310.1	444.3	3.40	2.03	379.1	523.9	1.38	0.17
Cr ₂₀ Mn ₂₀ Fe ₃₄ Co ₂₀ Ni ₆	141.3	283.2	425.8	3.70	2.36	331.5	458.9	1.38	0.22
Cr ₂₀ Mn ₂₀ Fe ₃₀ Co ₂₀ Ni ₁₀	136.9	276.3	418.2	3.75	2.42	321.7	442.6	1.37	0.23
Cr ₂₀ Mn ₂₀ Fe ₂₀ Co ₂₀ Ni ₂₀	128.5	262.5	402.6	3.85	3.12	284.8	404.6	1.42	0.29
Cr ₂₅ Fe ₂₅ Co ₂₅ Ni ₂₅	138.7	275.6	411.0	3.80	2.48	248.3	379.8	1.53	0.39

Table 3. Young's modulus E in several high-symmetry directions, the anisotropy factor of Young's modulus f_E , and the elastic anisotropy A_u of HEAs in the hcp and fcc phases.

$E = E([hkl])$ for all HEAs is shown in Fig. 1 for the hcp and fcc phases, in order of increasing f_E for the sake of comparison. The Young's modulus surface for the hcp phase is axially symmetric owing to the symmetry of the elastic constant tensor. Furthermore, we can see that there is a correlation between the magnitude of the anisotropy factor f_E and the shape of the $E([hkl])$ surface, e.g., hcp Cr₂₅Fe₂₅Co₂₅Ni₂₅ and fcc Cr₂₀Mn₂₀Fe₂₀Co₂₀Ni₂₀ are more anisotropic than hcp Cr₂₀Mn₂₀Fe₃₀Co₂₀Ni₁₀ and fcc Cr₁₀Mn₃₀Fe₅₀Co₁₀, respectively.

We derived the polycrystalline Young's modulus E , bulk modulus B , and shear modulus G employing the calculated single-crystal elastic constants, which were determined using the Voigt-Reuss-Hill average method³¹. Fig. 2 displays the polycrystalline moduli as a function of average valence electron concentration (VEC). From Fig. 2, we can see that all the moduli of the five HEAs in the hcp phase decrease with increasing VEC, and the variations are ~38% for G , ~36% for E , and ~26% for B . Turning to the fcc phase, it can be seen that E and G reduce until the VEC reaches ≈ 8 , then both slightly increase. We find that the decreases are about 20% and 16% for G and E , respectively. Nevertheless, for B , the variation is very small when the VEC is lower than 8, but it exhibits a large increase when the VEC approaches 8.25. Comparing these two phases, we observe that all presented HEAs in their hcp phase have larger E , B , G than in their fcc phase when the VEC ≤ 8 . Interestingly, fcc Cr₂₅Fe₂₅Co₂₅Ni₂₅ with a VEC of 8.25 has larger moduli compared with its hcp phase.

To get further insight into the elastic anisotropy in these HEAs, we compare the fcc and hcp phases. To this end, we employ a universal elastic anisotropy parameter A_u . Different from other anisotropy indicators, such as the commonly used Zener anisotropy ratio³², A_u allows direct comparison of the anisotropy of different crystal structures and is defined as³³.

$$A_u = 5 \frac{G_V}{G_R} + \frac{B_V}{B_R} - 6. \quad (3)$$

Here, the indexes V and R denote averaging through the Voigt and Reuss methods, respectively. It should be noted that $G_V \geq G_R$ and $B_V \geq B_R$ ^{31,34}, hence $A_u \geq 0$. For an isotropic crystal, A_u is zero, and its deviation from zero gives a measure of the anisotropy.

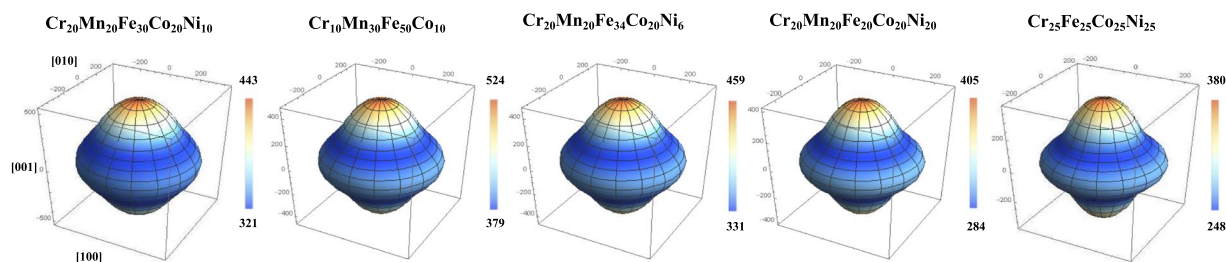
The derived values are summarized in Table 3. For the fcc phase, we observe that Cr₁₀Mn₃₀Fe₅₀Co₁₀ has the smallest A_u , whereas Cr₂₀Mn₂₀Fe₂₀Co₂₀Ni₂₀ has the largest one. This trend reflects that of f_E^{fcc} . For the hcp phase, A_u is close to zero and increases with increasing VEC. Comparing the two close-packed phases, we conclude that the fcc structure is elastically more anisotropic than the hcp structure. This result confirms two previous findings for elements and binary alloys, namely that for the same material, the anisotropy of the fcc phase exceeds that of the hcp phase³⁵, and the hexagonal crystal class is the class with least A_u ³³.

Ideal shear strength. The elastic constants and polycrystalline moduli considered so far describe the mechanical properties of materials in the small deformation region, where the stress-strain relations are linear. In the following, we go beyond the linear elasticity regime and consider the resistance of the ideal fcc and hcp single crystals against shear within the (111) and (0001) planes, respectively. The ideal strength is the applied stress at which a perfect crystal becomes mechanically unstable. It is an intrinsic property of a material and can provide insight into the correlation between chemical bonding and crystal symmetry. The ideal strength has been accepted as a mechanical parameter for the design of high performance materials^{36–38}. It has been demonstrated that the measured strengths approach the strengths obtained from first-principles electronic structure calculations in some cases^{38–42}, e.g., for whiskers. In this work, we selected two HEAs in the hcp structure, i.e., Cr₂₀Mn₂₀Fe₃₀Co₂₀Ni₁₀ and Cr₂₀Mn₂₀Fe₂₀Co₂₀Ni₂₀, and calculated their ideal shear strengths (ISSs) on the basal plane [(0001)] along the $[10\bar{1}0]$ direction. For Cr₂₀Mn₂₀Fe₂₀Co₂₀Ni₂₀ in the fcc phase, the ISS on the (111) plane along the $[11\bar{2}]$ direction was reported previously⁴³. It should be noted that the chosen shear systems in the fcc and hcp structures are equivalent, see Fig. 3 and discussion below. A monoclinic computational cell was employed to model the affine shear deformation, which is displayed in Fig. 3(a). The shear stress $\tau(\gamma)$ is given by

$$\tau(\gamma) = \frac{1}{\Omega(\gamma)} \frac{\partial E}{\partial \gamma}, \quad (4)$$

where E is strain energy per atom and $\Omega(\gamma)$ is the volume at each shear strain γ defined as the ratio of displacement along the $[10\bar{1}0]$ direction to the height of the unit cell. The first maximum on the stress-strain curve Eq. (4) determines the ISS τ_m with corresponding engineering maximum shear strain γ_m . Here, two modes of shearing were considered⁴⁴: (i) no relaxation is allowed after shearing; (ii) relaxation is allowed after each shear step, the

(a) hcp



(b) fcc

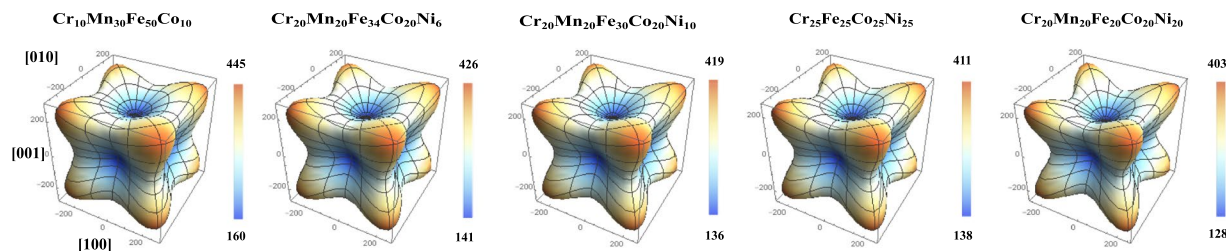


Figure 1. The directional dependence of Young's modulus E (in GPa) of HEAs in the hcp and fcc structures in the order of increasing f_E . The Cartesian axes specify the projection of E onto the [100], [010], and [001] crystallographic axes. For the hcp phase, the [001] direction of the plot is parallel to the [0001] direction of the hcp unit cell.

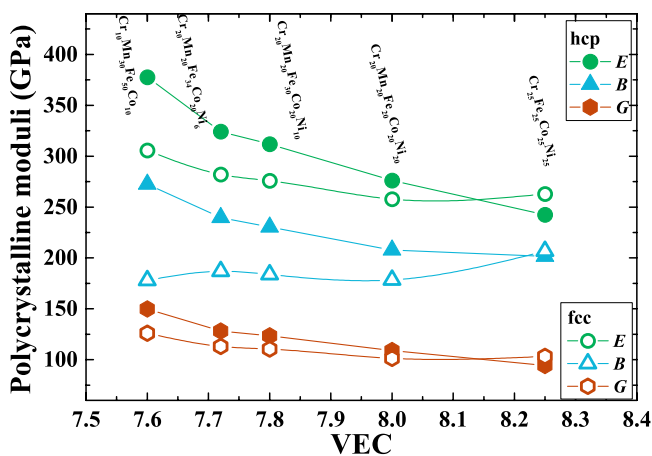


Figure 2. Polycrystalline moduli of the HEAs in the hcp and fcc phases as a function of their VEC.

only constraint being the shearing angle. (The underlying primitive unit cell governing the affine shear deformation contains one atom for the fcc phase and two atoms for the hcp phase. Relaxation involved volume and shape of the cell but a possible phonon instability was not investigated.)

Figure 3(c) presents the obtained stress-strain curves for $\text{Cr}_{20}\text{Mn}_{20}\text{Fe}_{30}\text{Co}_{20}\text{Ni}_{10}$ and $\text{Cr}_{20}\text{Mn}_{20}\text{Fe}_{20}\text{Co}_{20}\text{Ni}_{20}$. For the relaxed case, we found that the ISSs are 12.8 GPa and 11.7 GPa for $\text{Cr}_{20}\text{Mn}_{20}\text{Fe}_{30}\text{Co}_{20}\text{Ni}_{10}$ and $\text{Cr}_{20}\text{Mn}_{20}\text{Fe}_{20}\text{Co}_{20}\text{Ni}_{20}$, respectively. Compared to the relaxed ISSs, we realize that the ISSs neglecting lattice relaxation during shearing are 22% and 20% larger for $\text{Cr}_{20}\text{Mn}_{20}\text{Fe}_{30}\text{Co}_{20}\text{Ni}_{10}$ and $\text{Cr}_{20}\text{Mn}_{20}\text{Fe}_{20}\text{Co}_{20}\text{Ni}_{20}$, respectively. It is noteworthy that the obtained ISS of $\text{Cr}_{20}\text{Mn}_{20}\text{Fe}_{20}\text{Co}_{20}\text{Ni}_{20}$ in the hcp phase is more than two times larger than that in the fcc phase (4.4 GPa)⁴³, see Fig. 3(c). Moreover, compared to the fcc phase, the relaxation effect on the ISSs is less pronounced in the hcp phase, see Fig. 3(c).

The differences in the ISS can be explained as follows. Upon affine shear deformation, atoms in a close-packed layer gradually move over those in subjacent layers; see Fig. 3(a) and (b). For both the hcp and fcc structures this process involves atoms in two types of $(11\bar{2}0)$ and $(1\bar{1}0)$ planes, respectively. An atom moving over another atom (in adjacent close-packed layers) leads to a steeper increase in energy when they are located in the *same* type of $(11\bar{2}0)$ or $(1\bar{1}0)$ plane than when they are located in the *other* type of $(11\bar{2}0)$ or $(1\bar{1}0)$ plane. This is plausible since in the former case the two atoms directly move over one another, while in the latter case they are shifted by $1/2$

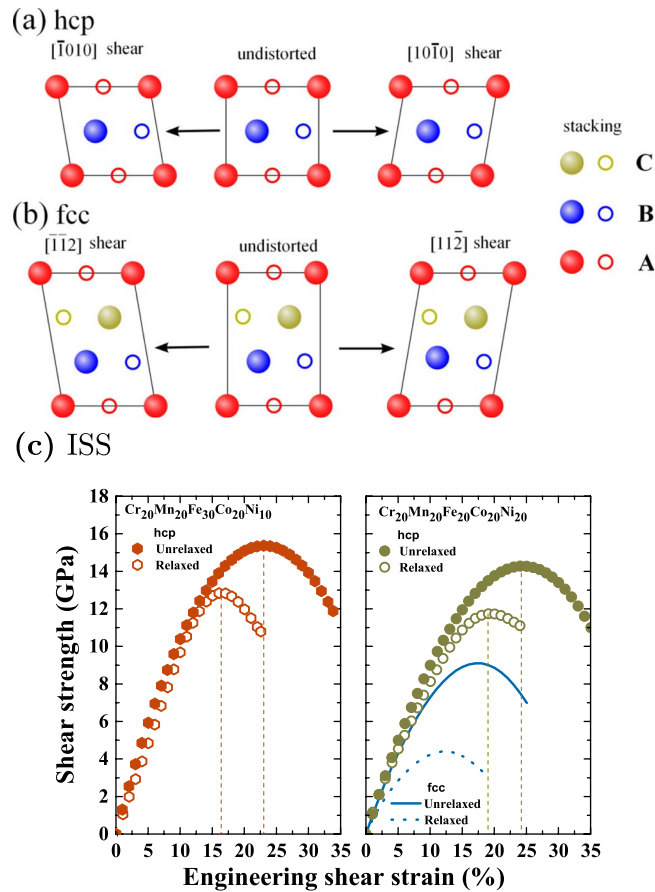


Figure 3. (a) Schematics of the $(0001)[10\bar{1}0]$ affine shear deformation of the hcp structure viewed along the $[11\bar{2}0]$ direction. The sheared conventional unit cell is monoclinic and contains four atoms. The $[10\bar{1}0]$ and $[\bar{1}010]$ shearing directions are equivalent. (b) Schematics of the $(111)[11\bar{2}]$ affine shear deformation of the fcc structure viewed along the $[1\bar{1}0]$ direction. The $[11\bar{2}]$ and $[\bar{1}\bar{1}2]$ shearing directions are not equivalent ($[11\bar{2}]$ is the soft direction, $[\bar{1}\bar{1}2]$ the hard one). In (a) and (b) the undistorted cells coincide with the orthorhombic representation of the hcp and the fcc structures, respectively. A, B, and C denote the stacking sequence, and filled and open circles distinguish atoms in the two types of $(11\bar{2}0)$ and $(1\bar{1}0)$ planes (these crystal planes lie in the figure plane). (c) The shear stress of hcp $\text{Cr}_{20}\text{Mn}_{20}\text{Fe}_{30}\text{Co}_{20}\text{Ni}_{10}$ and $\text{Cr}_{20}\text{Mn}_{20}\text{Fe}_{20}\text{Co}_{20}\text{Ni}_{20}$ under $(0001)[10\bar{1}0]$ shear deformation as a function of applied shear strain [corresponding to (a)]. The fcc data were taken from ref.⁴³.

$[11\bar{2}0]$ or $1/2[1\bar{1}0]$. In the case of shearing the hcp unit cell, an equal number of atoms moves over atoms located in the same type of $(11\bar{2}0)$ plane and located in the other type of $(11\bar{2}0)$ plane. This atomic displacement is independent of the shearing direction, i.e., $[10\bar{1}0]$ and $[\bar{1}010]$ are equivalent; see Fig. 3(a). When shearing the fcc structure in the $[11\bar{2}]$ direction, all atoms located in one type of $(1\bar{1}0)$ plane move over atoms located in the other type of $(1\bar{1}0)$ plane, whereas for shear in the opposite, $[\bar{1}\bar{1}2]$ direction all atoms located in one type of $(1\bar{1}0)$ plane move over atoms located in the same type of $(1\bar{1}0)$ plane. This leads to a steeper increase in energy and larger stress for shear in the $[\bar{1}\bar{1}2]$ direction (hard direction, τ_m^{hard}) than for shear in the $[11\bar{2}]$ direction (soft direction, τ_m^{soft}). Due to the ABAB stacking sequence, the shearing of the hcp structure may be viewed as being the intermediate case between these two limits. Thus, it is expected that the energy raises more rapidly (less rapidly) as a function of shear strain than in the soft (hard) direction of the fcc structure and the maximum shear stress is approximately given by the arithmetic average, $(\tau_m^{\text{hard}} + \tau_m^{\text{soft}})/2$. A previous DFT study for fcc Ni showed that $\tau_m^{\text{hard}} \approx 3\tau_m^{\text{soft}}$ ⁴⁵.

Half-width of the dislocation core. It has been recognized that the half-width of the dislocation core ζ plays an important role in the prediction of the Peierls stress⁴⁶. The half-width of the dislocation core ζ may be derived using the calculated ISS based on the following equation⁴⁶.

$$\zeta = \frac{Kb}{4\pi\tau_m}, \quad (5)$$

where b is the magnitude of the Burgers vector, and K is the energy factor of the dislocation. Here, we consider an edge dislocation in the basal plane (0001) with dislocation line along the $[10\bar{1}0]$ direction and Shockley partial Burgers vector $\mathbf{b} = \frac{1}{3}[10\bar{1}0]$. The corresponding energy factor K can be calculated viz⁴⁷,

$$K = (C + C_{13}) \left[\frac{C_{44}(C - C_{13})}{C_{33}(C + C_{13} + 2C_{44})} \right], \quad (6)$$

with

$$C = (C_{11}C_{33})^{1/2}. \quad (7)$$

The derived ζ are 1.57 Å and 1.53 Å for $\text{Cr}_{20}\text{Mn}_{20}\text{Fe}_{30}\text{Co}_{20}\text{Ni}_{10}$ and $\text{Cr}_{20}\text{Mn}_{20}\text{Fe}_{20}\text{Co}_{20}\text{Ni}_{20}$, respectively. It is found that the values of ζ for both HEAs are very close to their corresponding Burger vectors, i.e., 1.43 Å for $\text{Cr}_{20}\text{Mn}_{20}\text{Fe}_{30}\text{Co}_{20}\text{Ni}_{10}$ and 1.44 Å for $\text{Cr}_{20}\text{Mn}_{20}\text{Fe}_{20}\text{Co}_{20}\text{Ni}_{20}$. For fcc $\text{Cr}_{20}\text{Mn}_{20}\text{Fe}_{20}\text{Co}_{20}\text{Ni}_{20}$, ζ of an edge dislocation having a (111) glide plane with dislocation line along the $[1\bar{1}0]$ direction was calculated previously⁴³. It should be noted that the chosen edge dislocation configurations in the fcc and hcp close-packed planes are equivalent. Compared with the ζ of the hcp phase, the ζ of the fcc phase (3.89 Å) turns out to be more than two times larger. According to the Peierls-Nabarro model, a wider dislocation core combined with a similar Burgers vector leads to a reduced Peierls barrier⁴⁸. This result indicates that the fcc phase is more ductile than the hcp one.

Conclusion

In summary, a detailed first-principles investigation of the micro-mechanical properties of five polymorphic HEAs alloys in their fcc and hcp phases was presented. From the obtained elastic constants, it was found that all considered HEAs are elastically stable in both phases. We found that the polycrystalline moduli B , G , and E of the considered HEAs in the hcp phase decrease with increasing the VEC. The biggest and smallest variations were noticed in G and B , respectively. Turning to the fcc phase, we observed that E , G , and B show a non-monotonic behavior as a function of VEC. Comparing these two phases, we noticed that all presented HEAs in the hcp phase have larger E , B , and G when the VEC is below 8. We observed that the investigated HEAs are elastically more anisotropic in the fcc phase than in the hcp phase. We found that the obtained ISS for the selected $\text{Cr}_{20}\text{Mn}_{20}\text{Fe}_{20}\text{Co}_{20}\text{Ni}_{20}$ in its hcp phase is two times larger than in its fcc phase. In addition, the relaxation effect on the ISSs of the hcp phase was found to be less pronounced than that of the fcc phase. The calculated half-widths of the dislocation core for $\text{Cr}_{20}\text{Mn}_{20}\text{Fe}_{20}\text{Co}_{20}\text{Ni}_{20}$ suggested that the Peierls barrier in the hcp phase is larger than in the fcc phase. The present results are expected to offer a guideline for further developing high performance HEAs.

Methods

The first-principles method used in this study is based on density-functional theory (DFT)⁴⁹, and the Kohn-Sham equations were solved using the exact muffin-tin orbitals method (EMTO)^{50–52}. For the self-consistent determination of the charge density and the total energy calculations, we employed the Perdew-Burke-Ernzerhof functional⁵³. Here, all calculations were performed in the paramagnetic state, which was described by the disordered-local moment model⁵⁴. The problem of chemical disorder was treated within the coherent-potential approximation (CPA) and the total energy is computed via the full charge-density technique^{55,56}. The basis set included s, p, d, and f states. Brillouin zone integrations were performed on a $33 \times 33 \times 33$ and a $31 \times 31 \times 25$ k-points mesh for the fcc and hcp single-crystal elastic constants calculations, respectively. In this work, for the equation of state calculations, we used the primitive cell for the fcc and hcp phases. For the elastic constants calculations, the unit cell with highest symmetry compatible with the prescribed deformation (including the unstrained state) were employed; for further methodological details, see ref.⁵⁶. Based on the accuracy of our numerical fits to the computed energy versus strain curves and on the Brillouin zone sampling, all elastic parameters and ISSs are estimated to possess error bars below 1 GPa and 0.5 GPa, respectively. The accuracy of the EMTO-CPA method for the equation of state, elastic properties, and ideal strength of alloys has been demonstrated in a number of previous works^{57–59}.

References

1. Senkov, O. N., Senkova, S. V., Woodward, C. F. & Miracle, D. B. Low-density, refractory multi-principal element alloys of the Cr-Nb-Ti-V-Zr system: microstructure and phase analysis. *Acta Mater.* **61**, 1545–1557 (2013).
2. Wu, Y. D. *et al.* A refractory $\text{Hf}_{25}\text{Nb}_{25}\text{Ti}_{25}\text{Zr}_{25}$ high-entropy alloy with excellent structural stability and tensile properties. *Mater. Lett.* **130**, 277–280 (2014).
3. Guo, S., Ng, C., Wang, Z. & Liu, C. T. Solid solutioning in equiatomic alloys: Limit set by topological instability. *J. Alloys Compd.* **583**, 420–413 (2014).
4. Zou, Y., Maiti, S., Steurer, W. & Spolenak, R. Size-dependent plasticity in an $\text{Nb}_{25}\text{Mo}_{25}\text{Ta}_{25}\text{W}_{25}$ refractory high-entropy alloy. *Acta Mater.* **65**, 85–97 (2014).
5. Guo, W. *et al.* Local atomic structure of a high-entropy alloy: an x-ray and neutron scattering study. *Metall. Mater. Trans. A* **44A**, 1994–1997 (2013).
6. Li, Z., Pradeep, K. G., Deng, Y., Raabe, D. & Tasan, C. C. Metastable high-entropy dual-phase alloys overcome the strength-ductility trade-off. *Nature* **534**, 227–230 (2016).
7. Huang, S. *et al.* Mechanism of magnetic transition in FeCrCoNi-based high entropy alloys. *Mater. Des.* **103**, 71–74 (2016).
8. Niu, C., Zaddach, A. J., Koch, C. C. & Irving, D. L. First principles exploration of near-equiatomic NiFeCrCo high entropy alloys. *J. Alloys Compd.* **672**, 510–520 (2016).
9. Li, X., Tian, F., Schönecker, S., Zhao, J. & Vitos, L. Ab initio-predicted micromechanical performance of refractory high-entropy alloys. *Sci. Rep.* **5**, 12334 (2015).
10. Granberg, F. *et al.* Mechanism of radiation damage reduction in equiatomic multicomponent single phase alloys. *Phys. Rev. Lett.* **116**, 135504 (2016).

11. Otto, F., Yang, Y., Bei, H. & George, E. P. Relative effects of enthalpy and entropy on the phase stability of equiatomic high-entropy alloys. *Acta Mater.* **61**, 2628–2638 (2013).
12. Li, Z. & Raabe, D. Strong and ductile non-equiatomic high-entropy alloys: Design, processing, microstructure, and mechanical properties. *JOM* **21**, 1–8 (2017).
13. Zhao, Y. J. *et al.* A hexagonal close-packed high-entropy alloy: The effect of entropy. *Mater. Des.* **96**, 10–15 (2016).
14. Takeuchi, A., Amiya, K., Wada, T., Yubuta, K. & Zhang, W. High-entropy alloys with a hexagonal close-packed structure designed by equi-atomic alloy strategy and binary phase diagrams. *JOM* **66**, 1984–1992 (2014).
15. Yuzenko, K. V. *et al.* First hexagonal close packed high-entropy alloy with outstanding stability under extreme conditions and electrocatalytic activity for methanol oxidation. *Scripta Mater.* **138**, 22–27 (2017).
16. Feuerbacher, M., Heidelmann, M. & Thomas, C. Hexagonal high-entropy alloys. *Mater. Res. Lett.* **3**, 1–6 (2015).
17. Gao, M. C., Zhang, B., Guo, S. M., Qiao, J. W. & Hawk, J. A. High-entropy alloys in hexagonal close-packed structure. *Metall. Mater. Trans. A* **47A**, 3322 (2016).
18. Tracy, C. L. *et al.* High pressure synthesis of a hexagonal close-packed phase of the high-entropy alloy CrMnFeCoNi. *Nat. Commun.* **8**, 15634 (2017).
19. Zhang, F. *et al.* Polymorphism in a high-entropy alloy. *Nat. Commun.* **8**, 15687 (2017).
20. Zhang, F. X. *et al.* Pressure-induced fcc to hcp phase transition in Ni-based high entropy solid solution alloys. *Appl. Phys. Lett.* **110**, 011902 (2017).
21. Zhao, S., Stocks, G. M. & Zhang, Y. Stacking fault energies of face-centered cubic concentrated solid solution alloys. *Acta Mater.* **134**, 334–345 (2017).
22. Ma, D., Grabowski, B., Körmann, F., Neugebauer, B. & Raabe, D. Ab initio thermodynamics of the CoCrFeMnNi high entropy alloy: Importance of entropy contributions beyond the configurational one. *Acta Mater.* **100**, 90–97 (2015).
23. Gludovatz, B. *et al.* A fracture-resistant high-entropy alloy for cryogenic applications. *Science* **345**, 1153–1158 (2014).
24. Jin, K. *et al.* Tailoring the physical properties of Ni-based single-phase equiatomic alloys by modifying the chemical complexity. *Sci. Rep.* **6**, 20159 (2016).
25. Zaddach, A. J., Niu, C., Koch, C. C. & Irving, D. L. Mechanical properties and stacking fault energies of nifecrcomn high-entropy alloy. *JOM* **65**, 1780–1789 (2013).
26. Grimvall, G. *Thermophysical Properties of Materials* (North-Holland, Amsterdam, 1999).
27. Born, M. & Huang, K. *Dynamical theory of crystal lattices* (Oxford University Press, Oxford, 1954).
28. Ge, H., Song, H., Shen, J. & Tian, F. Effect of alloying on the thermal-elastic properties of 3d high-entropy alloys. *Mater. Chem. Phys.* **210**, 320–326 (2018).
29. Tsai, H. In Gale, W. F. & Totemeier, T. C. (eds.) *Smithells Metals Reference Book*, chap. 15 (Elsevier Butterworth-Heinemann, Burlington, 2004).
30. Tromans, D. Elastic anisotropy of hcp metal crystals and polycrystals. *Int. J. Res. Rev. Appl. Sci.* **6**, 462–483 (2011).
31. Hill, R. The elastic behaviour of a crystalline aggregate. *Proc. phy. Soc. A* **65**, 349–354 (1952).
32. Zener, C. *Elasticity and Anelasticity of Metals* (University of Chicago, Chicago, 1948).
33. Ranganathan, S. I. & Starzewski, M. O. Universal elastic anisotropy index. *Phys. Rev. Lett.* **101**, 055504 (2008).
34. Hill, R. Elastic properties of reinforced solids: Some theoretical principles. *J. Mech. Phys. Solids* **11**, 357–372 (1963).
35. Ledbetter, H. & Migliori, A. A general elastic-anisotropy measure. *J. Appl. Phys.* **100**, 063516 (2006).
36. Clatterback, D. M., Chrzan, D. C. & Morris, J. W. Jr. The ideal strength of iron in tension and shear. *Acta Mater.* **51**, 2271–2283 (2003).
37. Nagasako, N., Jahnátek, M., Asahi, R. & Hafner, J. Anomalies in the response of V, Nb, and Ta to tensile and shear loading: Ab initio density functional theory calculations. *Phys. Rev. B* **81**, 094108 (2010).
38. Kelly, A. & Macmillan, N. H. *Strong Solids* (Clarendon, Oxford, 1986).
39. Brenner, S. S. Tensile strength of whiskers. *J. Appl. Phys.* **27**, 1484–1491 (1956).
40. Lowry, M. B. *et al.* Achieving the ideal strength in annealed molybdenum nanopillars. *Acta Mater.* **58**, 5160–5167 (2010).
41. Lee, C., Wei, X., Kysar, J. W. & Hone, J. Measurement of the elastic properties and intrinsic strength of monolayer graphene. *Science* **321**, 385–388 (2008).
42. Kim, J. Y., Jang, D. & Greer, J. R. Tensile and compressive behavior of tungsten, molybdenum, tantalum and niobium at the nanoscale. *Acta Mater.* **58**, 2355–2363 (2010).
43. Li, X. *et al.* Tensile and shear loading of four fcc high-entropy alloys: a first-principle study. *Phys. Rev. B* **97**, 094102 (2018).
44. Ogata, S., Li, J. & Yip, S. Ideal pure shear strength of Aluminum and Copper. *Science* **298**, 807–811 (2002).
45. Liu, Y. L., Zhang, Y., Zhou, H. B., Lu, G. H. & Kohyama, M. Theoretical strength and charge redistribution of fcc Ni in tension and shear. *J. Phys.: Condens. Matter* **20**, 335216 (2008).
46. Joós, B. & Duesbery, M. S. The Peierls stress of dislocation: An analytic formula. *Phys. Rev. Lett.* **78**, 266–269 (1997).
47. Hirth, J. P. & Lothe, J. *Theory of Dislocations* (Wiley, New York, 1992).
48. Cai, W., Bulatov, V. V., Chang, J. P., Li, J. & Yip, S. Dislocation core effects on mobility. In Nabarro, F. & Hirth, J. (eds) *Dislocations in Solids*, vol. 12, chap. 64, 1–80 (Elsevier B.V., 2004).
49. Hohenberg, P. & Kohn, W. Inhomogeneous electron gas. *Phys. Rev.* **136**, B864–871 (1964).
50. Andersen, O. K., Jepsen, O. & Krier, G. In Kumar, V., Andersen, O. K. & Mookerjee, A. (eds.) *Lectures on Methods of Electronic Structure Calculations*, 63 (World Scientific, Singapore, 1994).
51. Vitos, L. Total-energy method based on the exact muffin-tin orbitals theory. *Phys. Rev. B* **64**, 014107 (2001).
52. Vitos, L., Skriver, H. L., Johansson, B. & Kollár, J. Application of the exact muffin-tin orbitals theory: the spherical cell approximation. *Comput. Mater. Sci.* **18**, 24–28 (2000).
53. Perdew, J. P., Burke, K. & Ernzerhof, M. Generalized gradient approximation made simple. *Phys. Rev. Lett.* **77**, 3865–3868 (1996).
54. Gyorfyy, B. L., Pindor, A. J., Staunton, J., Stocks, G. M. & Winter, H. A first-principles theory of ferromagnetic phase transitions in metals. *J. Phys. F: Met. Phys.* **15**, 1337–1386 (1985).
55. Gyorfyy, B. L. Coherent-potential approximation for a nonoverlapping-muffin-tin-potential model of random substitutional alloys. *Phys. Rev. B* **5**, 2382–2384 (1972).
56. Vitos, L. *Computational Quantum Mechanics for Materials Engineers* (Springer-Verlag, London, 2007).
57. Taga, A., Vitos, L., Johansson, B. & Grimvall, G. Ab initio calculation of the elastic properties of $\text{Al}_{1-x}\text{Li}_x$ ($x \leq 0.20$) random alloys. *Phys. Rev. B* **71**, 014201 (2005).
58. Vitos, L., Korzhavyi, P. A. & Johansson, B. Stainless steel optimization from quantum mechanical calculations. *Nat. Mater.* **2**, 25–28 (2003).
59. Li, X., Schönecker, S., Zhao, J., Johansson, B. & Vitos, L. Ideal strength of random alloys from first-principles theory. *Phys. Rev. B* **87**, 214203 (2013).

Acknowledgements

The Swedish Research Council, the Swedish Steel Producers' Association, the Swedish Foundation for Strategic Research, the Swedish Foundation for International Cooperation in Research and Higher Education, and the Hungarian Scientific Research Fund (research project OTKA 109570) are acknowledged for financial support. The simulations were performed on resources provided by the Swedish National Infrastructure for Computing (SNIC) at the National Supercomputer Centre in Linköping.

Author Contributions

X.L. designed the research and performed the calculations. X.L., D.L.I., and L.V. prepared the manuscript.

Additional Information

Competing Interests: The authors declare no competing interests.

Publisher's note: Springer Nature remains neutral with regard to jurisdictional claims in published maps and institutional affiliations.



Open Access This article is licensed under a Creative Commons Attribution 4.0 International License, which permits use, sharing, adaptation, distribution and reproduction in any medium or format, as long as you give appropriate credit to the original author(s) and the source, provide a link to the Creative Commons license, and indicate if changes were made. The images or other third party material in this article are included in the article's Creative Commons license, unless indicated otherwise in a credit line to the material. If material is not included in the article's Creative Commons license and your intended use is not permitted by statutory regulation or exceeds the permitted use, you will need to obtain permission directly from the copyright holder. To view a copy of this license, visit <http://creativecommons.org/licenses/by/4.0/>.

© The Author(s) 2018